A multiscale theory for mesenchymal cell migration in straight or curved channel confinement

Wenya Shu[1,2] and C. Nadir Kaplan[1−4 ∗]
[1]Department of Physics,
Virginia Polytechnic Institute and State University, Blacksburg, VA 24061, USA.
[2]Center for Soft Matter and Biological Physics,
Virginia Polytechnic Institute and State University, Blacksburg, VA 24061, USA.
[3]Department of Mechanical Engineering,
Virginia Polytechnic Institute and State University, Blacksburg, VA 24061, USA.
[4]Center for the Mathematics of Biosystems,
Virginia Polytechnic Institute and State University, Blacksburg, VA 24061, USA.
∗ To whom correspondence should be addressed: nadirkaplan@vt.edu

Mesencyhmal cells navigate the extracellular matrix *in vivo* by processing both its mechanical properties and confinement geometry. Here we develop a multiscale whole-cell theory to investigate cell spreading and migration in two-dimensional (2D) viscoelastic channel confinements of varying width and curvature. Our simulations show that, in straight channels, the cell migration speed depends monotonically on the substrate elastic stiffness, which is otherwise biphasic on an unconfined substrate. This is because confinement enforces directional spreading while reducing the spreading area, which results in lower intracellular viscous drag on the nucleus and a higher net traction force of polarized cells in our model. In contrast, we find that confinement curvature slows down cell migration since the friction forces between the bending cell and the confinement walls increase with curvature. We validate our model with experimental data for cell migration in straight microchannels spanning a wide range of ECM stiffness as well as in curved microchannels. Our model illuminates the intertwined effects of substrate viscoelasticity and confinement geometry on cell spreading and migration in complex microenvironments, paving the way for the design of scaffolds for controllable cell migration.

Keywords: Mechanobiology, Microchannels, Confinement, Curvature, Viscoelasticity

Significance statement: Cell migration occurs within a 3D extracellular matrix *in vivo*, which confines cell movement into narrow openings. However, most studies focus on migration on open surfaces, overlooking these extra constraints. Here, we develop a theory to reveal how the mechanical properties of the substrate and confinement geometry jointly regulate migration. Our model provides new insights into how cells navigate tissue openings *in vivo* or microchannels *in vitro*, and highlights how curves along the cells' trajectories modulate their migration efficiency. Our findings not only improve our understanding of cell motility in development, immune response, and cancer invasion, but also pave the way for the design of biomimetic platforms that control cell movement for tissue engineering and regenerative medicine.

INTRODUCTION

The extracellular matrix (ECM) is a complex 3D biopolymer network that mediates cell migration *in vivo*. Various experimental and theoretical studies have conventionally regarded the ECM as a 2D tissue culture surface, providing valuable mechanistic insights into how mesenchymal cells form focal adhesions, change shape, and migrate in response to the viscoelastic properties of the ECM [1–6]. However, the 3D ECM topography profoundly modifies the cell behavior from that observed on a 2D substrate, mainly by confining the cells into narrow openings [7–9]. To mimic the effect of 3D confinement on cell mechanics, experiments have commonly used microchannels *in vitro* and demonstrated that channel width, together with ECM elastic stiffness, alters migration behavior [10–14]. Recent experiments also highlighted how channel curvature regulates individual or collective cell migration [15, 16]. To this end, a comprehensive theory that explains the migration dynamics as a function of the channel viscoelasticity, confinement, and curvature can enhance our understanding of mesenchymal cell behavior inside the ECM *in vivo*.

Apart from the channel curvature, the individual effects of the ECM viscoelasticity and confinement on mesencymal migration have theoretically and computationally been investigated [17, 18]. The models rely on the fact that cell migration takes place through sequential, transient lamellipodial or filopodial grips on a substrate by virtue of singular focal adhesions (FAs). The cell gauges the intracellular actomyosin contractile forces to form and reinforce the FAs in the first place, which in turn transmit these forces to the ECM [2, 19, 20]. This dynamic interplay enables cells to actively perceive, react, and adapt to the changes in the ECM biomechanics. The motor-clutch model developed based on this reciprocal relationship between the FAs and actomyosin dynamics successfully elucidated cell adhesion and spreading on substrates with a wide range of elastic moduli and viscosities [4, 21–23]. By spatially connecting several motor-clutch modules to a central cell body, stochastic cell simulators explained the migration behavior on elastic and viscoelastic substrates without actomyosin-regulated FA reinforcement [3, 24–26]. Taking into account confinement, however, necessitates the integration of membrane and cytoskeletal mechanics to rigorously account for the contact forces between the cell and confinement boundaries while maintaining cell structural integrity. Finite element methods (FEM) and phase field models can robustly simulate steric effects associated with confinement barriers, e.g., in the context of adhesion-independent 3D amoeboid migration [27, 28]. Moreover, FEM and cellular Potts models can potentially tackle mesenchymal cell mechanics under confinement as with previous work involving unconfined 2D elastic substrates [29, 30]. Nevertheless, treating the singular profiles of the transient filopodia in FEM as well as modeling viscoelastic media in cellular Potts or phase-field models remain inherently challenging [26, 31, 32]. In contrast, vertex-based or agent-based models that represent the cell by a polygonal mesh provide a straightforward framework to incorporate the contact mechanics between a mesenchymal cell and a rigid barrier while enabling the treatment of substrate viscoelasticity and singular geometries of emergent filopodia during migration [33–36].

Here we generalize our vertex-based multiscale theory in Refs. [35, 36], which were developed for cells migrating on flat, unconfined substrates, to investigate the migration and spreading dynamics in straight or curved microchannels. Our model integrates subcellular motor-clutch dynamics at the FA sites that form between the cell and the viscoelastic substrate with the structural mechanics of intracellular components and the mechanics of lateral cell contact with channel walls. Our results demonstrate that strong confinement within straight channels significantly suppresses cell spreading but enhances migration speed, in quantitative agreement with experiments [13]. Particularly, on very stiff substrates under strong confinement, the cell spreads less, which alleviates the drag force on the nucleus. This leads to an increase in the net traction force of polarized cells, which in turn promotes the cell migration speed. As a result, the dependence of the migration speed on substrate stiffness becomes monotonic, as opposed to the nonmonotonic profiles observed for unconfined substrates. We alo find that increasing channel curvature elevates friction forces between the cell and confinement walls, thereby suppressing both the cell spreading area and migration

speed. We further reveal that highly curved channels can even impede cell migration, particularly on viscous substrates with high instantaneous stiffness. Altogether, we integrate the effect of ECM viscoelasticity and confinement geometry into a unified cell migration model that enhances our understanding of cell migration in straight, confined channels and unveils the regulatory role of channel curvature in cell migration.

METHODS

Cell migration relies on the coordinated interplay of subcellular processes including FA formation, actin polymerization, and actomyosin contraction, as well as the mechanical integrity maintained by structural components such as the cytoskeleton network and cell membrane. In addition to the impact of the ECM mechanical properties on these subcellular mechanisms, geometrical constraints within the microenvironment can directly regulate the deformation and distribution of cell structural components.

Here we extend our multiscale framework [35, 36], originally developed for mechanosensitive cell migration on viscoelastic substrates, to decipher the cell behavior in response to the combined effects of the ECM and confinement width and curvature. Our framework simplifies the migration dynamics to the directional cell spreading accompanied by the nucleus translocation in the absence of inertial effects since cells migrate in low-Reynolds-number environments. At the subcellular scale of our model, the spreading velocity of each vertex, which represents an FA site, is determined by a local force balance between the molecular clutches, membrane forces, and actomyosin contraction (Fig. 1A, B). We employ a chemomechanical coupling between the motor-clutch mechanism and the reaction–diffusion dynamics of the active and inactive Rac1 and RhoA GTPase proteins, whose asymmetric distributions can disrupt the front–rear symmetry of the cell and in turn polarize it. Because of confinement, mechanical equilibrium analysis at a vertex must include a contact detection feature to enforce nonpenetration into the rigid walls (Fig. 1 A), and account for increased contact forces on vertices due to cell bending in highly curved channels (Fig. 1 C). At the cellular level, the traction force at the FA sites, cytoskeletal elastic forces, and contact forces are transmitted to the nucleus. These forces collectively counteract the viscous drag force on the nucleus while the cell moves and drags the nucleus with it (Fig. 1A, D). The speed of nucleus motion is taken as the cell migration speed.

Equations of motion at subcellular scale

To update a vertex position $\mathbf{x}^i(t)$ in time t, the vertex spreading speed $\mathbf{V}_s^i \equiv \dot{\mathbf{x}}^i$ is determined from the local force balance at that vertex when the corresponding FA dynamics is known. The local force balance depends on whether or not a vertex contacts a channel wall. In the following, we first provide an overview of the spreading dynamics at a vertex as it was implemented in our previous models [35, 36]. Then, we detail its generalization that considers dynamic wall contact of a cell under confinement.

In our model, the radial component of the local spreading velocity $V_{s,n}^i = \mathbf{V}_s^i \cdot \hat{\boldsymbol{n}}^i$ is primarily dictated by the active forces associated with the FA mechanics that is regulated by the Rho GTPases, while the polar component $V_{s,\tau}^i = \mathbf{V}_s^i \cdot \hat{\boldsymbol{\tau}}^i$ relies on the balance between the polar component of the passive forces due to the cell membrane deformations and steric interactions, such as those from channel walls ($\hat{\boldsymbol{n}}^i$ and $\hat{\boldsymbol{\tau}}^i$ defined in Fig. 1A). The radial spreading speed is set by the competition between the actin polymerization rate V_p^i and the retrograde actin flow speed V_r^i, i.e., $V_{s,n}^i = V_p^i - V_r^i$ (Fig.1B). We compute V_r^i by employing a mean motor-clutch model at each vertex, which considers that proteins such as integrin, talin, and vinculin can form temporary molecular clutches with the ECM to generate adaptive traction while resisting actin retrograde flow (Sec. S1.1 in the Supporting Information) [21–23]. The adhesion reinforcement effect in our motor clutch model relates the clutch association rate k_{on}^i monotonically to the substrate elastic stiffness, which sets the local cell traction force strength F_{sub}^i and in turn determines the cell spreading area by

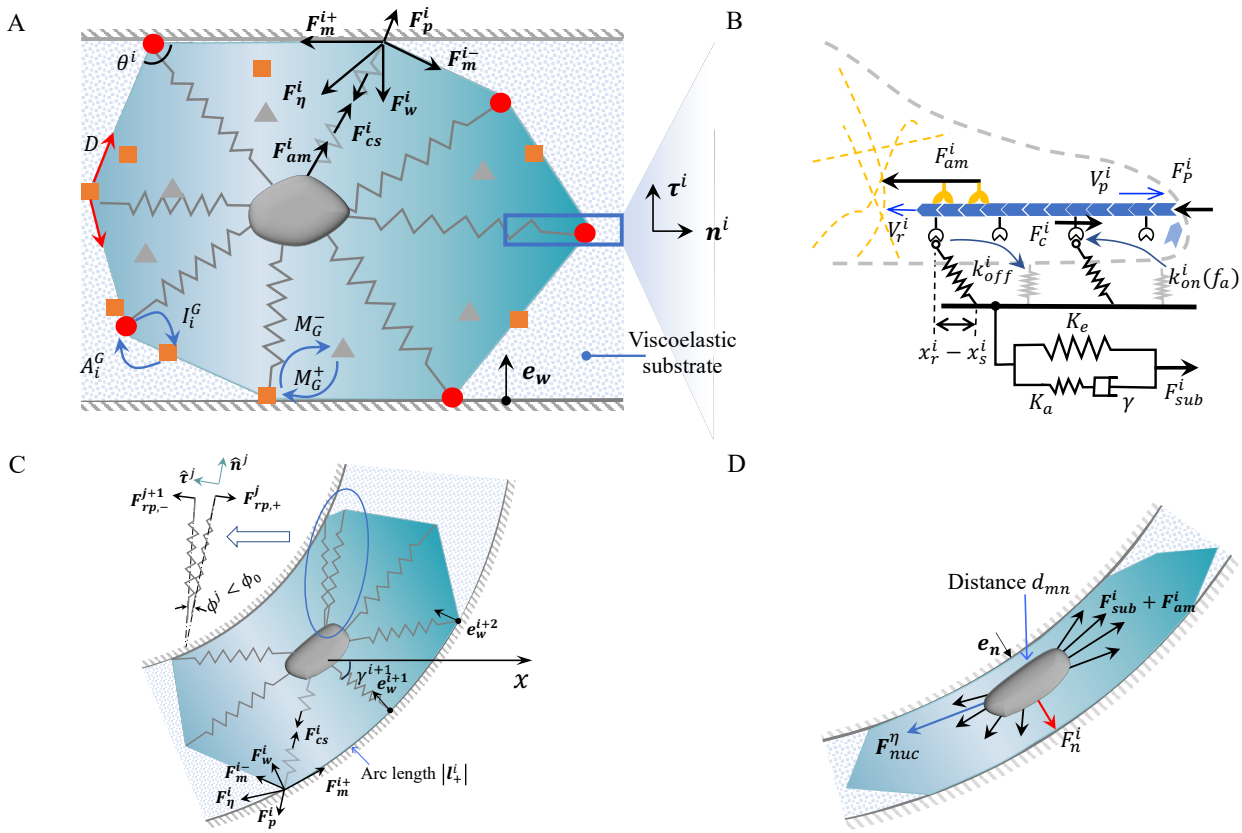

Figure 1: **Multiscale model for cell migration on a viscoelastic substrate in confinement.** (A) Chemical signaling pathways involve Rho GTPase proteins in active (red dots) or inactive state (orange squares) on the cell membrane, as well as dissolved in the cytoplasm in inactive form (gray triangles). The conversion rates between these states are A_G^i , I_G^i , M_G^- , M_G^+ (Eqs S16 and S17, Table S1). D : diffusion constant of the membrane-bound species. $\hat{\mathbf{n}}^i$, $\hat{\boldsymbol{\tau}}^i$: unit radial and polar vectors. (B) Motor-clutch model with stiffness-induced adhesion reinforcement. (C) A migrating cell bent in a curved channel. ϕ^i : angle between two adjacent cytoskeletal springs. When ϕ^i falls below the threshold ϕ_0, repulsive forces $\mathbf{F}_{rp,\pm}^i$ are triggered. $\mathbf{F}_\eta^i$: membrane-wall friction force, $\mathbf{F}_w^i$: wall reaction force, $\mathbf{e}_w^i$: normal vector to the channel wall γ^i angle between the x-axis and i-th cytoskeletal spring. (D) Forces on the cell nucleus in a highly curved channel. F_n^i : constraint force acting in the normal direction $\mathbf{e}_n$ that prevents the nucleus-membrane distance d_{mn} from falling below a threshold d_{min} . All other parameters and variables in (B)–(D) are defined in Table 1.

affecting $V_{s,n}^i$ (Sec. S1.1) [36]. To determine the direction of local spreading, we couple V_p^i and V_r^i to the Rac1 and RhoA proteins that undergo reaction and diffusion (Sec. S1.2); that way, our model facilitates emergent mechanical polarization of the cell from the dynamical chemical polarity of the Rho GTPases.

To explore how the ECM viscoelastic properties regulate cell spreading and movement, we adopt the standard linear solid (SLS) model for viscoelasticity. The SLS model comprises an elastic spring linked in parallel with a Maxwell arm (see Fig.1B), where K_e represents the residual elastic stiffness as $t \to \infty$ after the viscous stresses have relaxed, γ is the substrate viscosity, and K_a is the additional stiffness that governs the stress relaxation with a timescale $\tau_r \equiv \gamma/K_a$. In the limit $t \to 0$, the SLS model yields an instantaneous stiffness $K_{t\to 0} = K_e + K_a$ for the elastic response of the substrate before the viscous relaxation of the stress.

Maintaining the structural integrity of the cell to accurately characterize both the contact forces and substrate-stiffness-dependent cell spreading areas in our simulations requires that we consider force trans-

Table 1: **Model summary for cell migration without confinement.** V_0 : Unloaded retrograde flow speed, $\mathbf{F}^i_{am}$: active pulling force acting on the actomyosin complex, f_m : single myosin motor stall force, V^0_p : characteristic polymerization rate, N : number of vertices, k^i_{on}, k^i_{off} : rate constants of clutch association/dissociation (Sec. S1.1.1), N^0_c : reference molecular clutch number, F^i_{sub} : substrate deformation force, K_c : clutch stiffness, K_e, K_a, γ : SLS model parameters (Fig. 1B, Table 2), K^b_{cs} : baseline cytoskeletal stiffness, ΔK_{cs} : stiffness increment, β : Area-dependent nonlinearity coefficient, K_m : membrane stiffness, α , χ : shape factor parameters (Sec. S1.2.1), η^0_{cp} : reference cytoplasm viscosity, $\Delta\eta_{cp}$: cytoplasm viscosity increment, D : membrane-bound rho GTPase diffusion constant, a : active, in : inactive. For the numerical values of the parameters used in the simulations, see Table S1.

Cell spreading kinematics at a vertex i ($\hat{\mathbf{n}}^i$, $\hat{\boldsymbol{\tau}}^i$ unit radial and polar vectors; see Fig.1A)		
Vertex spreading speed $\boldsymbol{V}^i_s$	$\boldsymbol{V}^i_s = V^i_{s,n}\hat{\mathbf{n}}^i + V^i_{s,\tau}\hat{\boldsymbol{\tau}}^i$	-
Active radial spreading of a vertex $V^i_{s,n}$	$V^i_{s,n} = V^i_p - V^i_r$.	Eq. S1
Actin retrograde flow speed V^i_r	$V^i_r = \dot{x}^i_r = V_0\left(1 - \frac{F^i_{am}}{N^i_m f_m}\right)$, $F^i_{am} = \lvert\mathbf{F}^i_{am}\rvert = F^i_c - F^i_p$	Eq. S2
F-actin polymerization speed V^i_p	$V^i_p = \frac{R^i_a}{\langle R^i_a\rangle}V^0_p$, $\langle R^i_a\rangle = \sum R^i_a/N$, R^i_a : active Rac1	-
Active myosin motor number N^i_m	$N^i_m = N^0_m\frac{\rho^i_a}{\langle\rho^i_a\rangle}$, $\langle\rho^i_a\rangle = \sum\rho^i_a/N$, ρ^i_a : active RhoA	-
Motor-clutch model for the focal adhesion point at a vertex i		
Engaged clutch fraction P_i	$\frac{dP_i}{dt} = k^i_{\text{on}}(1-P^i) - k^i_{\text{off}}P^i$, $\quad 0 \le P_i \le 1$	Eq. S4
Total clutch force F^i_c	$F^i_c = F^i_{sub} = P^i N^i_c K_c(x^i_r - x^i_{xub})$, $N^i_c = \frac{R^i_a}{\langle R^i_a\rangle}N^0_c$	Eq. S5
Viscoelastic substrate deformation x^i_{sub}	$(K_e + K_a)\gamma\dot{x}^i_{sub} + K_a K_e x^i_{sub} = K_a F^i_{sub} + \gamma\dot{F}^i_{sub}$	Eq. S6
Membrane and fiber Hookean spring force ($\mathbf{x}^i$: vertex position vector)		
Cytoskeletal restoring force F^i_{cs}	$\frac{dF^i_{cs}}{dr^i} = K^b_{cs} + \Delta K_{cs}e^{\beta A}$, A : cell spreading area	Eq. S7
Membrane force $\mathbf{F}^i_{m,\pm}$	$\mathbf{F}^i_{m,\pm} = K_m(\mathbf{l}^i_\pm - \mathbf{l}_0)$, $\mathbf{l}^i_\pm \equiv \pm(\mathbf{x}^{i\pm1} - \mathbf{x}^i)$	-
The local force equilibrium at a vertex i		
Protrusion force at a vertex F^i_p	$F^i_p - F^i_{cs} + \left(\mathbf{F}^i_{m,+} + \mathbf{F}^i_{m,-}\right)\cdot\hat{\mathbf{n}}^{\mathbf{i}} - \eta_m l^i V^i_{s,n} = 0$	Eq. S8a
Vertex velocity at the polar direction $V^i_{s,\tau}$	$(\mathbf{F}^i_{m,+} + \mathbf{F}^i_{m,-})\cdot\hat{\boldsymbol{\tau}}^i - \eta_m l^i V^i_{s,\tau} = 0$	Eq. S8b
The net force balance at the nucleus		
Viscous drag force on the nucleus	$\mathbf{F}^\eta_{nuc} = -f_{shape}\mathcal{L}_{nuc}\eta_{cp}\dot{\mathbf{x}}_{nuc}$	-
Nucleus velocity $\dot{\mathbf{x}}_{nuc}$	$\sum_i(F^i_{sub} + F^i_{cs} - F^i_p)\hat{\mathbf{n}}^i + \mathbf{F}^\eta_{nuc} = 0$	Eq. S9, S13
Nucleus shape factor f_{shape}	$f_{shape} = 0.98\left(\chi A + 1\right)^{2\alpha}$	Eq. S11
Cytoplasm viscosity η_{cp}	$\eta_{cp} = \eta^0_{cp} + \Delta\eta_{cp}e^{\beta A}$	Eq. S12
Reaction and diffusion of Rac1 and RhoA		
Diffusive fluxes	$J^i_y \equiv -D(G^{i+1}_y/l^{i+1} - G^i_y/l^i)/\lvert\mathbf{l}^i_+\rvert$, $y = a$ or in	Eq. S14
The reaction-diffusion kinetics $G^i_a(t) \equiv \{R^i_a(t), \rho^i_a(t)\}$ $G^i_{in}(t) \equiv \{R^i_{in}(t), \rho^i_{in}(t)\}$ $G_{cp}(t) \equiv \{R_{cp}(t), \rho_{cp}(t)\}$	$\dot{G}^i_a = A^i_G G^i_{in} - I^i_G G^i_a + \left(J^{i-1}_a - J^i_a\right)$, $\dot{G}^i_{in} = -A^i_G G^i_{in} + I^i_G G^i_a + \left(J^{i-1}_{in} - J^i_{in}\right)$ $+ \frac{M^+_G G_{cp}}{N} - M^-_G G^i_{in}$, $\dot{G}_{cp} = -M^+_G G_{cp} + \sum_{i=1}^{N} M^-_G G^i_{in}$.	Eq. S15

mission between adjacent vertices and between each vertex and the nucleus (Sec. S1.1). To link the nucleus to the peripheral vertices, our framework represents the cytoskeleton as a set of nonlinear hyperelastic springs that incorporate strain stiffening. To represent each membrane section between adjacent vertices, we consider a linear spring with stiffness K_m and friction constant η_m to account for its friction with the ECM. The vertex local equilibrium condition contains all these components to determine the spreading velocity $\mathbf{V}_s^i$ (Table 1). However, when a vertex and the connected cell membrane section contact a rigid channel wall, the steric interactions restrict the vertex movement and concurrently augment the membrane-wall friction force, which significantly modify the local force balance as we describe next.

Vertex contact with straight channel walls. For a cell migrating in a rigid, straight channel, once the vertex i contacts the channel wall, the reaction force from the wall F_w^i must result in zero vertex speed in the normal direction to the wall $\hat{\mathbf{e}}_w$ (Fig. 1A). Moreover, contact between the membrane and the wall increases the local friction force. Therefore, we assume an augmented drag coefficient $\eta_m^i = (1+\epsilon)\,\eta_m$ to account for the enhanced friction during the movement of vertex i. Additionally, during contact, the membrane itself becomes more resistant to deformations due to a higher friction force. To accommodate this, we introduce an enhanced membrane stiffness denoted as $K_m^i = (1+\epsilon)K_m$. The value $\epsilon = 0.5$ was chosen based on experimental fits on the migration speed of U373-MG human glioma cells in straight channels (Sec. S2, Fig. S1) [13]. Then, the following equilibrium equations with the nonpenetration condition at the vertex i must hold:

$$F_p^i - F_{cs}^i + F_w^i(\hat{\mathbf{e}}_w \cdot \hat{\boldsymbol{n}}^i) + \left(\mathbf{F}_{m,+}^i + \mathbf{F}_{m,-}^i\right) \cdot \hat{\boldsymbol{n}}^i - \eta_m^i l^i V_{s,n}^i = 0\,, \tag{1a}$$

$$F_w^i(\hat{\mathbf{e}}_w \cdot \hat{\boldsymbol{\tau}}^i) + \left(\mathbf{F}_{m,+}^i + \mathbf{F}_{m,-}^i\right) \cdot \hat{\boldsymbol{\tau}}^i - \eta_m^i l^i V_{s,\tau}^i = 0\,, \tag{1b}$$

$$V_{s,n}^i(\hat{\boldsymbol{n}}^i \cdot \hat{\mathbf{e}}_w) + V_{s,\tau}^i(\hat{\boldsymbol{\tau}}^i \cdot \hat{\mathbf{e}}_w) = 0\,. \tag{1c}$$

The membrane forces at the ith vertex are given as $\mathbf{F}_{m,\pm}^i = K_m^i\left(\mathbf{l}_\pm^i - \mathbf{l}_0\right)$. Here, $\mathbf{l}_\pm^i \equiv \pm(\mathbf{x}^{i\pm1} - \mathbf{x}^i)$ are the distance vectors between vertex i and its two neighbors, and $\mathbf{l}_0$ is the initial distance between two adjacent vertices. In Eqs. 1a and 1b, the variable $l^i \equiv (|\mathbf{l}_+^i| + |\mathbf{l}_-^i|)/2$ defines the average membrane length about the ith vertex. Eq. 1a determines the membrane force resisting protrusion F_p^i and the radial spreading speed $V_{s,n}^i$ together with Eq. S1, S2, and S5 (Table 1), Eq.1b determines the polar spreading speed $V_{s,\tau}^i$, and Eq.1c sets the reaction force from the wall F_w^i by coupling the active and passive dynamics at vertex i to satisfy the nonpenetration condition.

Vertex contact with curved channel walls. In curved channels, the reaction forces at the cell-wall interface must counterbalance the internal forces that are generated due to the bending of the cells. This is because, under confinement, the mechanicaly stable state of the cell is a straight, elongated configuration along its polarization direction due to its structural integrity, which is collectively maintained by the cytoskeletal network, contractile actomyosin tension, and membrane resistance as included in our model. To test the curvature dependence of these contact forces, we perform FEM simulations of a bending elastic beam that represents an elongated cell within a curved channel (Sec. S3). We find that the reaction forces (equivalent to the contact forces) at the cell-wall interface have a quadratic dependence on the channel curvature as dictated by symmetry under the curvature sign change (Fig. S2). Since our vertex-based model represents the cell as a cable-truss structure without any inherent bending stiffness, we explicitly introduce a curvature-dependent stiffness to the cell membrane as

$$K_m^i = \left(1 + \epsilon + \mu\kappa^2\right) K_m\,, \tag{2}$$

where $\mu = 2 \times 10^4\ \mu m^2$ was determined through an iterative model calibration to match the experimental elongation length measurements of MDA-MB-231 cells in a circular channel with a radius $R = 50\ \mu m$ (see Sec. S2 and Fig. S3) [15]. Because the curvature-dependent reaction forces must also raise the membrane-

wall friction forces during migration, we introduce a modified drag coefficient

$$\eta_m^i = \left(1 + \epsilon + \mu\kappa^2\right)\eta_m \,. \tag{3}$$

Noting that the modified membrane forces are given by $\mathbf{F}_{m,\pm}^i = K_m^i\left(\mathbf{l}_\pm^i - \mathbf{l}_0\right)$ per Eq. 2, the spreading-induced friction forces are given by $\mathbf{F}_\eta^i = \eta_m^i l^i \mathbf{V}_s^i$ per Eq. 3, and the normal vector of the curved surface changes with the vertex position (e.g., $\hat{\mathbf{e}}_w^{i+1} \neq \hat{\mathbf{e}}_w^{i+2}$; Fig. 1C). Then, the force balance at a vertex i with a nonpenetration condition in a curved channel is written as

$$F_p^i - F_{cs}^i + F_w^i(\hat{\mathbf{e}}_w^i \cdot \hat{\boldsymbol{n}}^i) + \left(\mathbf{F}_{m,+}^i + \mathbf{F}_{m,-}^i\right)\cdot\hat{\boldsymbol{n}}^i - \eta_m^i l^i V_{s,n}^i = 0\,, \tag{4a}$$

$$F_w^i(\hat{\mathbf{e}}_w^i \cdot \hat{\boldsymbol{\tau}}^i) + \left(\mathbf{F}_{m,+}^i + \mathbf{F}_{m,-}^i\right)\cdot\hat{\boldsymbol{\tau}}^i - \eta_m^i l^i V_{s,\tau}^i + \left(F_{rp,+}^i + F_{rp,-}^i\right) = 0\,, \tag{4b}$$

$$V_{s,n}^i(\hat{\boldsymbol{n}}^i \cdot \hat{\mathbf{e}}_w^i) + V_{s,\tau}^i(\hat{\boldsymbol{\tau}}^i \cdot \hat{\mathbf{e}}_w^i) = 0\,. \tag{4c}$$

The last term including $F_{rp,\pm}^i$ on the left-hand side of Eq. 4b represents repulsive forces in the polar direction. These forces are incorporated to prevent the adjacent cytoskeletal elements from overlapping or crossing in highly curved channels. The computation of these repulsive forces is based on the penalty method from contact mechanics, which implies that the force is applied only when the angle ϕ_i becomes smaller than a threshold value ϕ_0 (Sec. S4). In general, $F_{rp,\pm}^i = 0\,pN$ for most vertices.

Eqs. 1a-4c complement Eq. S8 to calculate the spreading velocities $\mathbf{V}_s^i$ simultaneously for all vertices, which are in or without contact with the channel walls at a given time. That way, the model takes into account the long-range influence of contact forces to distant vertices without contact in that the local forces are transmitted not only to the neighboring vertices through the cell membrane, but also to the distant vertices through the cytoskeletal network over the cell nucleus, as detailed in the following.

Equation of motion of the nucleus

Our model represents the motion of the cell body by the translation of its nucleus. The linkage between the cytoskeleton and nucleus facilitates the transmission of various forces (Fig. 1A, D), including the cytoskeletal elastic forces $\mathbf{F}_{cs}^i$ and the active force resisting actomyosin contraction $\mathbf{F}_{am}^i$ (Fig. 1B, Table 1). The sum of these cytoskeletal and peripheral forces lead to the nucleus deformation and movement [37]. The nucleus velocity $\dot{\mathbf{x}}_{nuc}$ is computed by the balance between these forces and the viscous drag force within the cytoplasm that is given as $\mathbf{F}_\eta^i = -f_{shape}\mathcal{L}_{nuc}\eta_{cp}\dot{\mathbf{x}}_{nuc}$, where f_{shape} is the shape factor that measures the deviation of the nucleus from a perfect sphere with $f_{shape} = 1$, $\mathcal{L}_{nuc} = 6\pi r_{nuc}^0$ and r_{nuc}^0 is the radius of the undeformed spherical nucleus, and η_{cp} is the cytoplasm viscosity (Eq. S9 and Table 1). This relation implies that when the shape factor $f_{shape} = 1$, the viscous force reduces to the Stokes drag. Since cell spreading can significantly deform the nucleus and increase the cytoplasm viscosity, we related both the shape factor f_{shape} and the cytoplasm viscosity η_{cp} to the spreading area (Eqs. S11-S12, Table 1) [38–40]. This contributes to an augmented viscous drag force on the nucleus with increasing cell spreading area, hampering the cell migration speed on high-stiffness substrates in the absence of confinement [36].

In extremely curved channels, cell bending and elongation in our model may lead to a contact between the nucleus and the cell membrane. This is nonphysical since the nucleus and the cell membrane are typically separated by multiple layers of other cellular components, with the minimum distance between the nucleus surface and the cell surface being typically around 1 μm [37, 41]. Therefore, if the distance between the nucleus and membrane (d_{mn} in Fig.1E) falls below a minimum value of d_{min}, we introduce a constraint force F_n to enforce a zero velocity for the nucleus in the direction normal to the membrane ($\mathbf{e}_n$ in Fig. 1E). This gives an updated equilibrium system:

$$\dot{\mathbf{x}}_{nuc} \cdot \hat{\mathbf{e}}_n = 0 \quad \text{if} \quad d_{mn} \leq d_{min}\,, \tag{5a}$$

$$\sum_{i=1}^{N} \left(F_{sub}^{i} + F_{cs}^{i} - F_{p}^{i}\right) \hat{\boldsymbol{n}}^{i} + F_n \hat{\mathbf{e}}_n - f_{shape} \mathcal{L}_{nuc} \eta_{cp} \dot{\mathbf{x}}_{nuc} = 0\,, \quad F_n \begin{cases} > 0\,, & \text{if } d_{mn} \leq d_{min}\,, \\ = 0, & \text{otherwise.} \end{cases} \tag{5b}$$

Eq. 5a determines the contact force in Eq. 5b if $d_{mn} \leq d_{min}$, and Eq. 5b yields the nucleus velocity $\dot{\mathbf{x}}_{nuc}$.

Simulation procedure

We represent the initial vertex configuration of the cell as a regular polygon with $N = 16$ sides due to its decent convergence properties as with our previous work [35, 36]. All initial forces, velocities, displacements, and substrate deformations are set to zero. Since chemical signaling drives cell polarization followed by directional locomotion on uniform substrates, we enforce a nonuniform and stochastic initial distribution of the active Rac1 protein volume fraction, R_i^a, with higher values at random vertices at the cell front to mimic the random nature of the protrusion formations in the mesenchymal cells [35]. Likewise, a polarized and stochastic initial distribution of the active RhoA protein volume fractions ρ_i^a is taken with accumulation at the cell rear (manual polar symmetry breaking). In contrast, the initial conditions for R_{in}^i, ρ_{in}^i are uniform at time $t = 0$, and the cytoplasmic form R_{cp}, ρ_{cp} can be determined from the total volume fraction conservation (Sec. S5). This initial condition of Rho GTPase proteins contributes to the polarization and directed cell migration on unconfined substrates and along the direction of the confined channels. Starting from these initial conditions, we update the radial spreading speed of each vertex by solving the mean-field motor-clutch model (Eqs. S1–S6, Table 1). The calculation of the spreading velocity requires a contact condition assessment between a vertex and the channel wall: When a vertex is not in contact with the wall, Eq. S8a,b are used. Otherwise, Eqs. 1a–1c and Eqs. 4a–4c are used for vertex in contact with straight or curved channels, respectively. The nucleus velocity is calculated by solving Eq. S13 or Eq. 5a–5b, depending on its proximity to the cell membrane (d_{mn} in Fig. 1D). Meanwhile, the Rho-GTPase volume fractions are updated by solving the reaction and diffusion system in Eqs. S14, S15 by following the algorithm in Fig. S5. When the cytoplasmic inactive Rac1 volume fraction R_{cp} reaches a steady state, we reinitialize R_a^i and ρ_a^i stochastically to mimic the random nature of the protrusion formations in the mesenchymal cells. All fixed simulation parameters are listed in Table S1. The range of channel geometric parameters and ECM viscoelastic properties, which are of interest in this study, are provided in Table 2.

We present the simulation results in dimensionless form by using a position scale $L \equiv 2\pi r_0 = 2\pi \times 3\mu m$, speed scale $V_0 = 120\ nm/s$ (unloaded retrograde flow speed; Table S1), migration timescale $T \equiv L/V \approx 160\ s$, and force scale $F_0 \equiv N_m^0 f_m = 200\ pN$. Each simulation is run over $M > 10^6$ time steps with a time step of $\Delta t \approx 10^{-3}\ s$ ($\Delta t \approx 10^{-5}$ in dimensionless units), corresponding to the migration dynamics over at least an hour in real units. The spreading area, A, and the aspect ratio, δ, are determined as the average cell area and the average ratio of the cell's shortest axis to its longest axis, respectively, calculated over the last 10^6 time steps of the simulation. We define the migration speed V as the nucleus trajectory length $X \equiv |\mathbf{x}_{nuc}(M\Delta t) - \mathbf{x}_{nuc}(0)|$ divided by the total time $t_{total} \equiv M\Delta t$, i.e., $V \equiv L/t_{total}$. For each set of the ECM parameters and geometric factors (Table 2), we run n simulations to compute the sample mean spreading area, $\overline{A}$, and the mean migration speed, $\overline{V}$. The effects of the ECM parameters and geometric factors on the migration dynamics are validated by the experiments in Refs. [13, 15].

Table 2: **Material and geometric parameters.** The parameters K_e, K_a, γ are defined in Fig. 1B.

Symbol	Parameters	Dimensional	Dimensionless
K_e	Elastic stiffness	0.1-120 pN/nm [13, 21, 22]	$5\pi - 6000\pi$
K_a	Additional stiffness	$1.0 - 20\ pN/nm$ [22]	$50\pi - 1000\pi$
γ	Viscosity	$0.1 - 100.0\ pN{\cdot}s/nm$ [22]	$0.06 - 60$
W	Channel width	$8 - 40\ \mu m$ [13]	$0.4 - 2$
κ	Channel curvature	$0 - 0.02\ 1/\mu m$	$0 - 0.4$

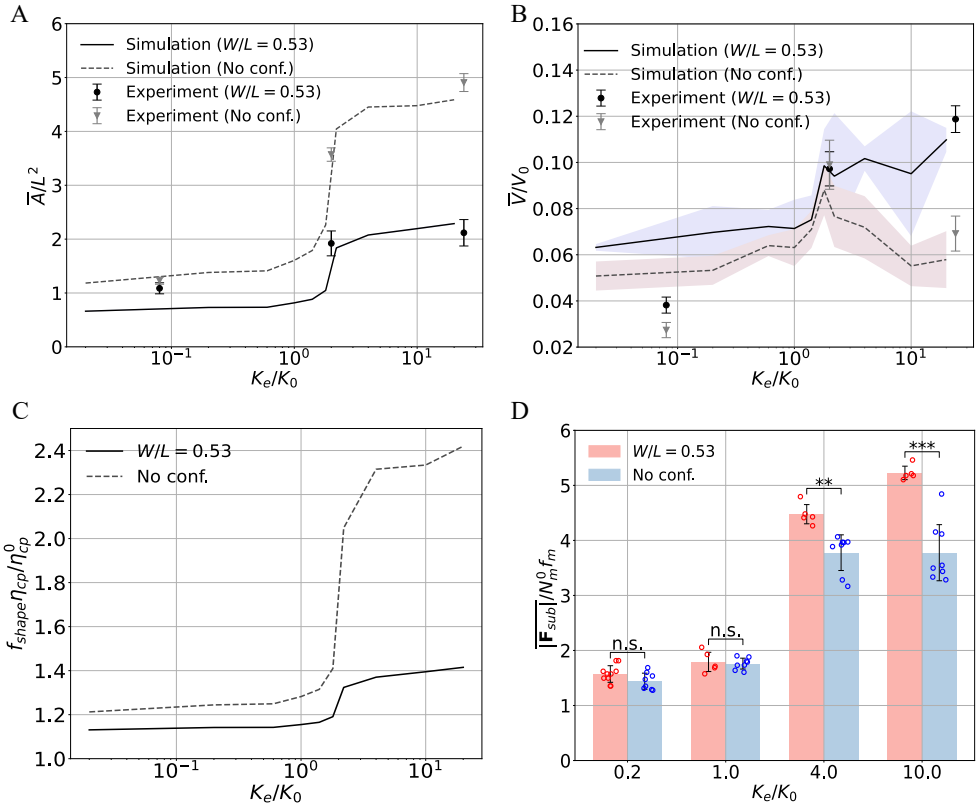

Figure 2: **Matrix confinement suppresses cell spreading and promotes migration speed.** (A) Unitless mean spreading area $\overline{A}/L^2$ and its standard deviation versus the uniform unitless elastic stiffness of a substrate, K_e/K_0 , for cells migrating in a confined channel (full line, $W/L = 0.53$). The characteristic threshold stiffness $K_0 \equiv N_m^0 f_m k_{on}^0/V_0 \approx 5\ pN/nm$ classifies the substrate as 'stiff' when $K_e > K_0$ and 'soft' when $K_e \leq K_0$ (Sec. S1). The dashed line shows the dependence of $\overline{A}/L^2$ on the stiffness of an unconfined substrate. (B) Unitless migration speed $\overline{V}/V_0$ and its standard deviation as a function of the substrate elastic stiffness K_e for fixed channel width $W/L = 0.53$. The dashed line is the biphasic stiffness/mean speed relation on uniform substrates without spatial confinement [36]. (C) Viscous drag coefficient of the nucleus $f_{shape}\eta_{cp}/\eta_{cp}^0$ versus K_e/K_0 on unconfined substrates and within confined microchannels. The calculation of f_{shape} and η_{cp} depends on the computed spreading area (Eqs. S11, S12, Table 1). (D) Comparison between the mean net traction forces ($|\overline{\mathbf{F}_{sub}}| = |\sum_{i=1}^{N} \mathbf{F}_{sub}^i|$) of cells migrating on unconfined substrates and within confined microchannels as a function of unitless substrate stiffness. Statistical analysis is performed for each pair of results with the statistical significance (p) denoted as: $***: p < 0.001$, $**: p < 0.01$, $*: p < 0.05$, and n.s.: $p > 0.05$ (Sec. S6). In (A) and (B), the mean values and the standard deviations are calculated over $n = 10$ simulations, while dots and error bars show the experimental data from Ref. [13] [42].

Results

Effect of confinement on cell spreading and migration

We first investigate the impact of physical confinement in a straight channel on the areal spreading and migration speed of cells on elastic substrates (i.e., viscosity $\gamma \to 0$). Regardless of channel confinement, cell spreading area on elastic substrates consistently increases with substrate stiffness due to the adhesion reinforcement effect (Fig. 2A). However, since the reaction force F_w^i on a vertex that is contact with a channel wall leads to an increasing radial protrusion force F_p^i at that vertex (see Eqs. 1a and 4a), the radial spreading speed $V_{s,n}^i$ of the vertex decreases (see Eq. S1-S2). As a result, channel confinement significantly suppresses cell spreading, reproducing the experimental data obtained from U373-MG human glioma cells on polyacrylamide hydrogels [13]. This suppression is more pronounced on stiffer substrates because increased substrate stiffness promotes greater cell spreading, resulting in higher reaction forces (F_w^i) from the channel walls. Consequently, the areal spreading is significantly reduced on stiff substrates ($K_e > K_0 \equiv N_m^0 f_m k_{on}^0 / V_0 = 5pN/nm$) compared to the softer ones ($K_e < K_0$) (Fig. 2A). Channel confinement not only quantitatively affects migration speed but also qualitatively governs migration behavior (Fig. 2B). Introducing confinement on a stiff substrate boosts the cell migration speed, transforming the biphasic speed-stiffness relationship on unconfined substrates into a monotonic profile. One underlying reason is the suppression of the areal spreading in confined channels, which decreases both the shape factor f_{shape} (Eq. S11) and the cytoplasm viscosity η_{cp} (Eq. S12). As a result, confinement inhibits the increase of the viscous drag force on the nucleus, thereby promoting faster migration with increasing stiffness (Fig. 2C). Additionally, confinement on very stiff substrates ($K_e \gg K_0$) not only induces cell elongation within the channel but also aligns the cytoskeletal elements at the front and rear of a migrating cell (see Movie 1). This is supported by the experiments that demonstrate an alignment within the intracellular distribution of phosphorylated myosin light chain and F-actin [13]. As traction forces become increasingly aligned, confinement enhances the net traction force of polarized cells on stiff substrates (Fig. 2D), effectively promoting cell migration speed and contributing to the monotonic speed-stiffness relationship.

We next explore the impact of channel width on cell migration speed at constant substrate stiffness. Note that our simulations employ persistent polarization along the channel wall characterized by a well-defined leading edge with polarized chemical signaling. This is an Ansatz; after all the influence of confinement on chemical polarity remains poorly understood in the existing literature. Our findings demonstrate that narrower channels promote faster migration on stiff and very stiff substrates, in agreement with the experiments for U373-MG human glioma cell migration (Fig. 3A, B) [13]. The influence of confinement on migration speed is particularly significant on very stiff substrates ($K_e/K_0 \gg 1$, Fig.3B). This is because confinement has a more pronounced influence on cell areal spreading and the net traction forces of polarized cells on very stiff substrates (Fig. 2B, D). On very stiff substrates, narrower channel widths lead to highly suppressed cell spreading and a very small cell aspect ratio δ, defined as the ratio of the shortest axis to the longest axis in the cell (Fig. 3C). The dependence of δ on the unitless width W/L is approximately linear (Fig. S7). Suppressed spreading significantly reduces the viscous drag on the nucleus as well (full line-circle in Fig. 3D). The net traction force increases linearly with decreasing aspect ratio because of the reduced radial dispersion of traction forces (Fig. 3E). In contrast, due to the limited effect of confinement on cell spreading and polarization on less stiff substrates, the reduction in the viscous drag coefficient is less pronounced (dashed diamond line, Fig. 3D), and the net traction force of polarized cells increases only marginally (Fig. 3F). This explains the varying impact of channel width on cells migrating on substrates with different stiffness. Although the above results are built upon the assumption of a well-defined cell leading edge with polarized chemical signaling, the enhancing effect of confinement on cell migration speed persists even when directional migration with persistent polarity is absent, as computed for randomly distributed initial chemical signaling (Fig. S8).

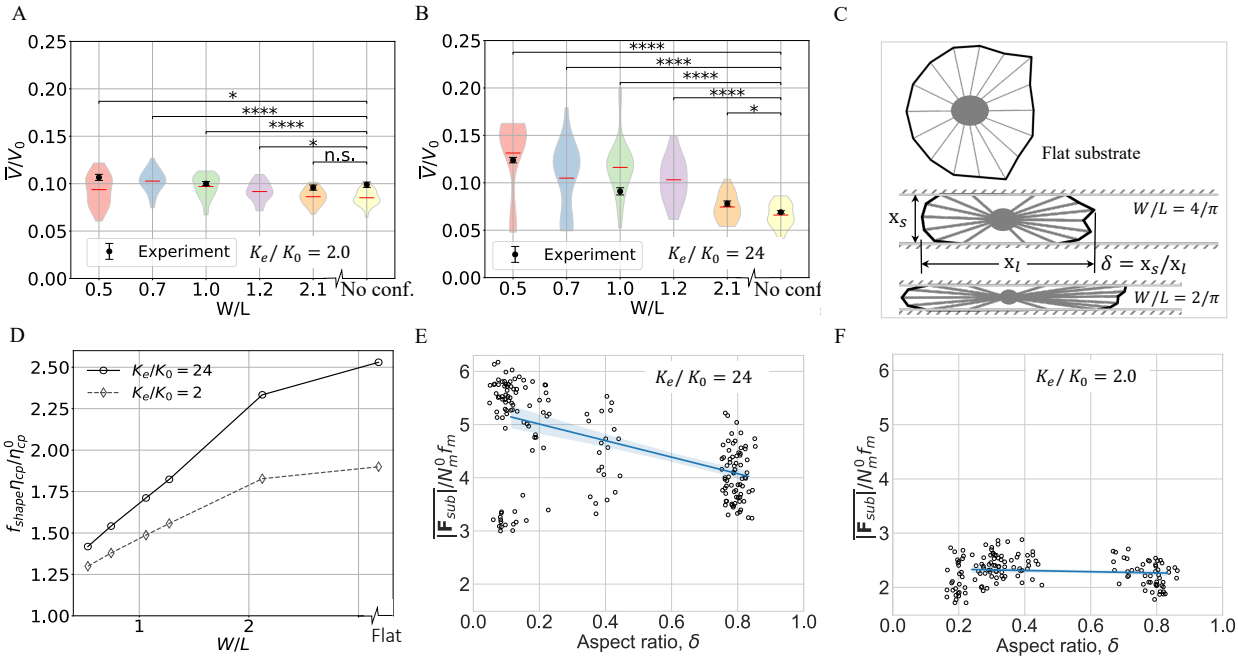

Figure 3: **Effect of channel width on migration speed.** Violin plots of $\overline{V}/V_0$ in straight channels as a function of the unitless channel width W/L for the substrate stiffness values (A) $K_e/K_0 = 2$, (B) $K_e/K_0 = 24$. Dots with error bars indicate the experimental data for the U373-MG human glioma cells [13]. The bar in the middle of each violin represents its arithmetic mean over more than $n > 20$ simulations (Fig. S6). Data are compared to the unitless migration speed without confinement. The p-values for statistical significance are represented by asterisks: $***: p < 0.001$, $**: p < 0.01$, $*: p < 0.05$, and n.s.: $p > 0.05$ (Sec. S6). (C) Influence of confinement on cell polarization and morphology on very stiff substrates with $K_e/K_0 = 24$. The aspect ratio δ is defined as the ratio of the cell short axis X_s to its long axis X_l. (D) Unitless viscous drag coefficient of the nucleus $f_{shape}\eta_{cp}/\eta_{cp}^0$ versus W/L for $K_e/K_0 = 2$ and 24. (E), (F) Unitless mean net traction force $\overline{|\mathbf{F}_{sub}|}/N_m^0 f_m$ as a function of δ for (E) $K_e/K_0 = 24$ (F) $K_e/K_0 = 2$. In (E), (F), the lines are linear fits with a translucent 95% confidence interval band. Each dot labels single simulation result.

Compared to persistent migration with robust polarity, cell migration under random signaling exhibits lower speeds. Notably, the increase in the mean migration speed with confinement is accompanied by an increase in the variance (Fig. S8B). This is because the net traction forces in confined channels experience larger fluctuations due to the randomness of the polarization direction (Fig. S8C).

Effect of channel curvature on cell spreading and migration

We next focus on the simulations of cells in curved channels to investigate the influence of curvature on cell spreading and migration speed. Our model predicts that cells exhibit reduced spreading and slower migration in channels with smaller radii or, equivalently, higher curvatures (Fig.4A, B). This can be attributed to the increase in the friction forces between the cell membrane and the wall due to the stronger contact reaction forces when a cell bends more in higher curvature channels (Movie 2). Consequently, the membrane encounters greater resistance to deformation, and the mobility of the vertices in contact with the channel walls becomes progressively hindered. The influence of curvature becomes more prominent on substrates with higher stiffness. This is because the contact length between the membrane and the wall increases with larger spreading areas on stiffer substrates, leading to higher friction forces (Movie 3). With a smaller

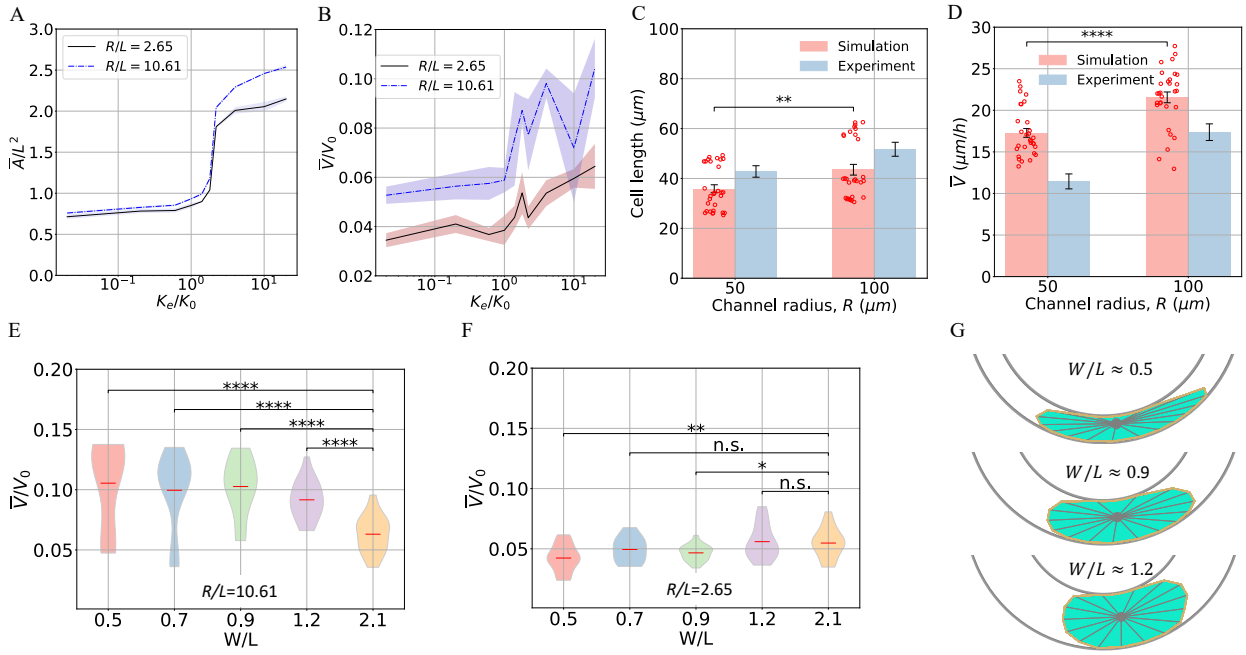

Figure 4: **Channel curvature suppresses both spreading and migration.** (A) Unitless mean spreading area $\overline{A}/L^2$ versus unitless substrate elastic stiffness K_e/K_0. (B) Unitless mean migration speed $\overline{V}/V_0$ and its standard deviation as a function of K_e/K_0 . The mean and standard deviation are calculated over $n = 5$ simulations at each data point. (C), (D) Comparison of our simulations with the experiments in Ref. [15] for (C) cell length and (D) migration speed in curved channels with different radii of curvature ($R = 50\ \mu m$ and $100\ \mu m$). The microchannels have a fixed width $W = 8\ \mu m$ and a fixed substrate stiffness $K_e = 8\ pN/nm$, which correspond to the experimental parameters. Data in different channel radii are compared using t-test ($n \approx 20$), where $***$: $p < 0.001$, $**$: $p < 0.01$ (Sec. S6). The scatter plots display all results from simulations, with the standard deviations depicted as error bars. (E), (F) Violin plots of $\overline{V}/V_0$ versus channel width w/L for the channel radii (E) $R/L = 10.61$ ($R = 200\mu m$) and (F) $R/L = 2.65$ ($R = 50\mu m$), each for constant substrate stiffness $K_e/K_0 = 24$. The bar in each violin represents its arithmetic mean. To compare the data with wide channels ($W/L = 2.1$), a t-test was conducted with significance levels denoted by: $****$: $p < 0.001$, $**$: $p < 0.01$, $*$: $p < 0.05$, and n.s. (not significant) ($p > 0.05$). (G) Representative cell shapes in curved channels with different confinement widths ($R = 50\ \mu m$).

membrane-wall dissipation coefficient μ (Eq. 3), we observed the reduced influence of channel curvature on cell spreading and migration speed (see Fig. S9). This verifies the critical role of the friction forces in the regulation of cell migration in curved channels.

To validate our predictions, we compared our simulations to the experiments for MDA-MB-231 cells migrating in curved microchannels [15]. To match the experimental setup, the simulated channels have a constant width of $W = 8\ \mu m$, and two different channel radii with $R = 50\ \mu m$ and $R = 100\ \mu m$. The substrate stiffness is taken to be $K_e = 8\ pN/nm$, corresponding to a Young's modulus of $E_{sub} \approx 8\ kPa$ used in the experiments [15] [42]. It is evident that both the cell length and migration speed in channels with higher curvatures decrease significantly, in agreement with experiments (Fig. 4C, D).

To further investigate the interplay between confinement and curvature in the regulation of cell migration, we vary the channel width in curved channels. We consider a very stiff substrate ($K_e/K_0 = 24$) and two different unitless channel curvatures $R/L = 10.61$ and $R/L = 2.65$. For low curvature, narrower channel widths result in faster cell migration (Fig.4E), as with our prediction for straight channels (cf. Fig.3B).

However, in highly curved channels ($R/L = 2.65$), increasing confinement does not promote faster migration (Fig. 4F). The observed difference can be primarily attributed to the enhanced friction forces between the cell membrane and the channel walls in more curved channels. It is evident that increasing confinement can increase friction forces due to the contact of more vertices with the walls, leading to a longer contact length of the cell membrane (Fig. 4G). In highly curved channels, which are characterized by a large friction coefficient (η_m^i in Eq.3), cells encounter a substantial increase in the friction forces against the membrane, which largely overrides the effect of channel width and hinders migration as shown in (Fig. 4FG). In contrast, in channels with small curvature, the friction coefficient between the membrane and the channel walls remains low, similar to that in straight channels. As a result, migration speed continues to increase due to the concurrent reduction in the viscous drag force on the nucleus and the increase in the net traction force as the channel width decreases (Fig. S10).

Combined effect of confinement geometry and matrix viscoelasticity on migration

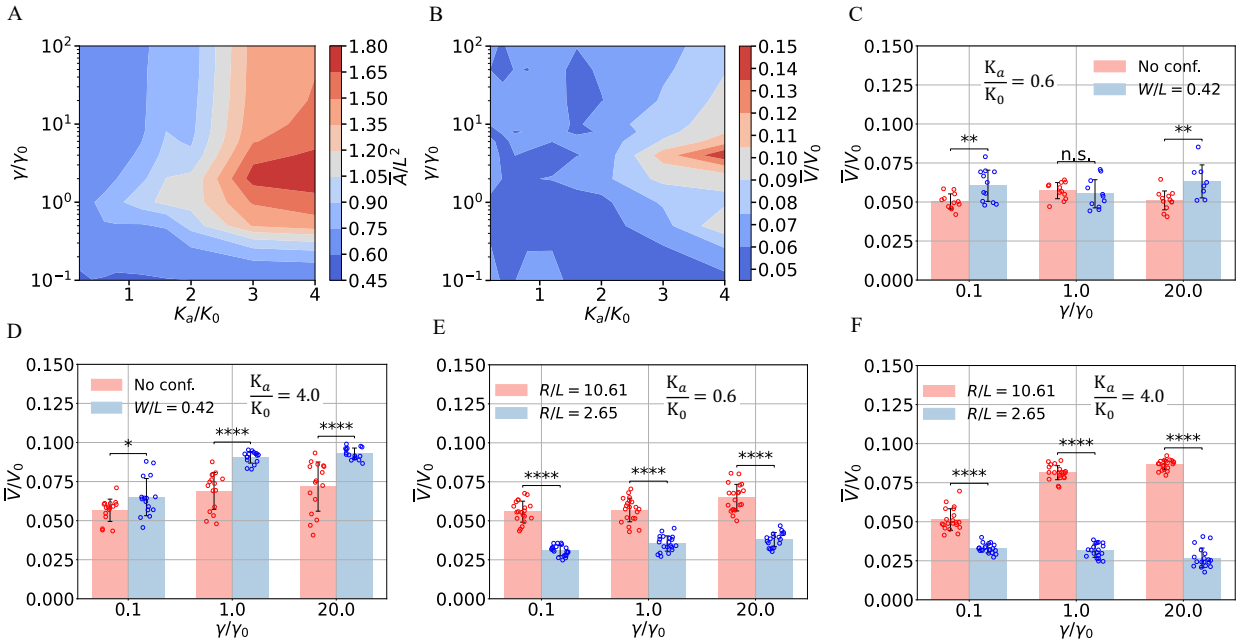

Figure 5: **Effect of confinement and its curvature on cell spreading and migration on viscoelastic substrates.** Contour plots of (A) the unitless mean cell area $\overline{A}/L^2$ and (B) the unitless mean migration speed $\overline{V}/V_0$ as a function of the unitless additional stiffness K_a/K_0 and unitless substrate viscosity γ/γ_0 in a straight channel for a width $W/L = 0.42$ and long-term stiffness $K_e/K_0 = 0.02$ ($\gamma_0 = K_0/k_{on}^0 \approx 1\ pN \cdot s/nm$). The contour plot contains 100 data points with $n \geq 5$ simulations at each point. For unitless additional stiffness values (C) $K_a/K_0 = 0.6$, (D) $K_a/K_0 = 4.0$, comparison between $\overline{V}/V_0$ on unconfined substrates and in channels ($W/L = 0.42$) over different γ/γ_0. For (E) $K_a/K_0 = 0.6$ and (F) $K_a/K_0 = 4.0$, comparison of $\overline{V}/V_0$ in channels with different curvatures as a function of γ/γ_0. A paired t-test was performed in (C)-(F) to determine the statistical significance ($n \approx 20$), where $***: p < 0.001$, $**: p < 0.01$, $*: p < 0.05$, and n.s.: $p > 0.05$ (Sec. S6). In (C)-(F), each dot represents one simulation result (error bars: standard deviation).

We further sought to understand the effect of substrate viscoelasticity on cell migration in the presence of different geometric constraints. In this setting, viscosity influences migration by modulating the short-

term mechanical response through the instantaneous stiffness $K_{t\to 0} = K_e + K_a$. Here we set the long-term substrate stiffness $K_e/K_0 = 0.02$ and instead varied K_a to modulate $K_{t\to 0}$ (Fig. 5A). This approach is justified because viscoelastic effects are most pronounced when K_e is small; for large K_e, $K_{t\to 0}$ remains nearly constant, reducing the impact of the viscosity γ. On substrates with a low instantaneous stiffness ($K_{t\to 0} < K_0 = 5pN/nm$), the cell spreading area has a biphasic response to the viscosity. It reaches its maximum at an optimal viscosity ($\gamma_0 = K_a/k_{on}^0 \approx 1pN \cdot s/nm$; Fig. S11). In contrast, on substrates with high instantaneous stiffness ($K_{t\to 0} > K_0$), the activation of adhesion reinforcement leads to enhanced cell spreading (Fig. S10). These findings are consistent with previous studies on cell spreading dynamics on viscoelastic substrates without spatial confinement [22, 36]. Additionally, in a straight channel, a cell tends to reach its maximum migration speed on viscous substrates with a high instantaneous stiffness, where cells have large spreading areas (Fig.5A, B). Compared with cell migration on unconfined substrates, the results also indicate that straight channels can enhance migration speed, particularly on viscous substrates (Fig.5C, D). The underlying mechanism can again be attributed to the close correlation between cell spreading and migration in straight channels. Confinement effectively increases the cell anisotropy when cells spread to large areas, leading to decreasing aspect ratios with increased net traction forces (Fig. S12A). An in-depth computational analysis further confirms the linear negative correlation between the cell migration speed and the aspect ratio (Fig. S12B).

Last, we investigate the impact of channel curvature on cell migration on substrates with varying viscoelastic properties. An increase in curvature leads to a notable decrease in the cell migration speed (Fig. 5E, F), which is particularly pronounced for cells on substrates with high instantaneous stiffness and viscosity (Fig. 5F). This trend can be attributed to a bigger friction coefficient associated with higher curvature (Eq. 3). Additionally, on viscous substrates with high instantaneous stiffness, the larger spreading cells exhibit increased contact areas with the walls, resulting in amplified frictional forces (Movie 4).

Discussion

Mesenchymal migration dynamics strongly depends on the interactions between the cell and the mechanics and interstitial geometry of the ECM. However, how these factors regulate cell migration remains unclear due to the absence of a theoretical framework that considers the contact mechanics of a migrating cell in compliance with such a complex microenvironment. To bridge this theory gap, we have developed a multiscale theory that integrates cell-matrix interactions, cell-wall contact mechanics, and intracellular chemomechanical dynamics. Our model illuminates the mechanisms governing cell migration on viscoelastic substrates in straight or curved confinement.

Our model replicates the experiments for the cell spreading area and migration speed in straight microchannels in Ref. [13] as a function of substrate stiffness and channel width. Our results present two key findings for constrained migration on very stiff substrates: First, strong confinement (low channel width) reduces spreading, resulting in a lower viscous drag on the nucleus. Second, anisotropic spreading enforced by the channel walls aligns the traction forces across neighboring FA sites, increasing the net traction force along the migration direction. These two factors transform the typical biphasic relationship between the cell speed and stiffness of unconfined substrates into a monotonic relationship in straight channels.

Our simulations also uncover the impact of channel curvature on cell migration. We find that cells migrate less efficiently and spread over a smaller area in channels with higher curvatures, in agreement with experiments [15]. This phenomenon arises from the augmented friction forces between the cell membrane and channel walls. As the cells migrate in curved channels, the reaction forces from the channel walls grow nonlinearly to counteract cell bending and thereby induce a higher friction at the cell-wall interface (Eq. 3). Highly curved and narrow channels substantially impede cell migration speed by merging the effects of

an elevated friction coefficient with an increasing contact length. Consequently, the impact of increased confinement on migration speed is preempted by the channel curvature and even becomes detrimental. As a result, channel curvature shifts the positive correlation between the migration speed and confinement into a negative one where migration speed decreases with lower channel width.

We further explored the combined effect of confinement geometry and substrate viscoelasticity on cell spreading and migration dynamics. We find that confinement does not alter the relationship between the cell spreading area and substrate viscoelasticity, in alignment with our previous results for migration on unconfined substrates [36]. Specifically, cells in a straight confinement attain their maximum spreading area at the same optimal viscosity with that on flat, unconfined substrates. On the other hand, a decrease in straight channel width generally enhances the migration speed, particularly on viscous substrates with high instantaneous stiffness. This effect is again attributed to the enhanced net traction force experienced by the highly polarized cell. Furthermore, highly curved, narrow channels suppress the cell migration speed due to the increasing friction forces. This effect is particularly pronounced on viscous substrates with high instantaneous stiffness, where cells have a larger contact length with the channel walls.

While our model demonstrates that the interplay among the cell traction forces, viscous drag on the nucleus, and friction forces from the channel walls can explain the impact of the microchannel geometry on cell migration, it is important to note that cell migration *in vivo* may involve additional critical factors, considering both the complexity of geometric features and the inherent mechanisms of migration. One such example is when cells are in very confined spaces with sizes comparable to the nucleus ($W/L < 0.3$); the mesenchymal cell can then switch to an adhesion-free amoeboid phenotype where cell migration is predominantly controlled by the actin retrograde flow, and FA formation is altogether missing [12, 14, 43, 44]. Investigating how confinement can induce such a shift in the migration mode is an intriguing avenue for future research. Additionally, the influence of curvature on cell migration may involve biochemical and molecular mechanisms: Recent work suggests that curvature regulates cell motility through the redistribution of cytoskeletal molecules at the curved microchannel walls and accelerate the actin retrograde flow [15]. Further investigations into these mechanisms are necessary to achieve a more holistic understanding of curvature-driven effects on the cell behavior. Finally, the ECM microstructure exhibits important architectural features, such as matrix porosity and fiber alignment. Although microchannel studies offer valuable insights into cell migration within confined spaces, they cannot fully capture the complexity of the ECM's fibrillar structure. Understanding how the heterogeneous and anisotropic architecture of the ECM influences cell movement will require advanced modeling approaches and experimental methodologies [27, 45–47].

Conclusion

In conclusion, we have presented a multiscale theory for the migration of mesenchymal cells in complex microenvironments, including factors such as channel confinement, curvature, and ECM mechanical properties. Our multiscale model explains experimental spreading and migration data in straight and curved channels [13, 15]. Furthermore, we offer experimentally testable predictions for the combined influence of ECM viscoelasticity and confinement geometry on cell spreading and migration. Overall, our computational framework delivers valuable physical insights into how the ECM mechanics and geometric constraints jointly regulate mesenchymal migration.

Supporting Information. Supplementary text, 12 figures, and a table are available in the appended PDF document.

Movie 1. Cell migration on elastic substrates with varying stiffness under confinement ($W/L = 0.53$ channel width).

Movie 2. Cell migration in curved channels with $R/L = 2.65$ and $R/L = 10.61$ on an elastic substrate with stiffness $K_e/K_0 = 4$.

Movie 3. Cell migration in highly curved channels with different substrate stiffnesses $K_e/K_0 = 2$ and $K_e/K_0 = 20$.

Movie 4. Cell migration in highly curved channels with different substrate viscoelasticities $\gamma/\gamma_0 = 0.1$ and $\gamma/\gamma_0 = 10$.

Author Contributions. W.S.: conceptualization, formal analysis, investigation, software, validation, visualization, writing – original draft, review and editing; C.N.K.: conceptualization, formal analysis, project administration, resources, validation, writing – original draft, review and editing.

Declaration of Interests. The authors declare no competing interest.

Acknowledgments. We thank the College of Science and the Center for Mathematics of Biosystems at Virginia Tech for financial support.

Data availability. The source codes of the simulations can be downloaded at https://github.com/nadirkaplan/confined_migration.

References

[1] Theresa A Ulrich, Elena M de Juan Pardo, and Sanjay Kumar. "The mechanical rigidity of the extracellular matrix regulates the structure, motility, and proliferation of glioma cells". In: *Cancer research* 69.10 (2009), pp. 4167–4174.

[2] Bin Chen, Baohua Ji, and Huajian Gao. "Modeling active mechanosensing in cell–matrix interactions". In: *Annual review of biophysics* 44 (2015), pp. 1–32.

[3] Yuan Qin, Yuhui Li, Li-Yuan Zhang, and Guang-Kui Xu. "Stochastic fluctuation-induced cell polarization on elastic substrates: A cytoskeleton-based mechanical model". In: *Journal of the Mechanics and Physics of Solids* 137 (2020), p. 103872.

[4] Bo Cheng, Min Lin, Yuhui Li, Guoyou Huang, Hui Yang, Guy M Genin, Vikram S Deshpande, Tian Jian Lu, and Feng Xu. "An integrated stochastic model of matrix-stiffness-dependent filopodial dynamics". In: *Biophysical journal* 111.9 (2016), pp. 2051–2061.

[5] Ovijit Chaudhuri, Luo Gu, Max Darnell, Darinka Klumpers, Sidi A Bencherif, James C Weaver, Nathaniel Huebsch, and David J Mooney. "Substrate stress relaxation regulates cell spreading". In: *Nature communications* 6.1 (2015), pp. 1–7.

[6] Valeria Panzetta, Sabato Fusco, and Paolo A Netti. "Cell mechanosensing is regulated by substrate strain energy rather than stiffness". In: *Proceedings of the National Academy of Sciences* 116.44 (2019), pp. 22004–22013.

[7] Lucas T Vu, Gaurav Jain, Brandon D Veres, and Padmavathy Rajagopalan. "Cell migration on planar and three-dimensional matrices: a hydrogel-based perspective". In: *Tissue Engineering Part B: Reviews* 21.1 (2015), pp. 67–74.

[8] Katrina M Wisdom, Kolade Adebowale, Julie Chang, Joanna Y Lee, Sungmin Nam, Rajiv Desai, Ninna Struck Rossen, Marjan Rafat, Robert B West, Louis Hodgson, and Ovijit Chaudhuri. "Matrix mechanical plasticity regulates cancer cell migration through confining microenvironments". In: *Nature communications* 9.1 (2018), p. 4144.

[9] Kenneth M Yamada and Michael Sixt. "Mechanisms of 3D cell migration". In: *Nature Reviews molecular cell biology* 20.12 (2019), pp. 738–752.

[10] Eric M Balzer, Ziqiu Tong, Colin D Paul, Wei-Chien Hung, Kimberly M Stroka, Amanda E Boggs, Stuart S Martin, and Konstantinos Konstantopoulos. "Physical confinement alters tumor cell adhesion and migration phenotypes". In: *The FASEB Journal* 26.10 (2012), p. 4045.

[11] Hua Zhang, Ruixia Hou, Peng Xiao, Rubo Xing, Tao Chen, Yanchun Han, Penggang Ren, and Jun Fu. "Single cell migration dynamics mediated by geometric confinement". In: *Colloids and Surfaces B: Biointerfaces* 145 (2016), pp. 72–78.

[12] Anne Reversat, Florian Gaertner, Jack Merrin, Julian Stopp, Saren Tasciyan, Juan Aguilera, Ingrid De Vries, Robert Hauschild, Miroslav Hons, Matthieu Piel, Andrew Callan-Jones, Raphael Voituriez, and Michael Sixt. "Cellular locomotion using environmental topography". In: *Nature* 582.7813 (2020), pp. 582–585.

[13] Amit Pathak and Sanjay Kumar. "Independent regulation of tumor cell migration by matrix stiffness and confinement". In: *Proceedings of the National Academy of Sciences* 109.26 (2012), pp. 10334–10339.

[14] Yan-Jun Liu, Maël Le Berre, Franziska Lautenschlaeger, Paolo Maiuri, Andrew Callan-Jones, Mélina Heuzé, Tohru Takaki, Raphaël Voituriez, and Matthieu Piel. "Confinement and low adhesion induce fast amoeboid migration of slow mesenchymal cells". In: *Cell* 160.4 (2015), pp. 659–672.

[15] Yan Liu, Tianyu Zhao, Zhao Xu, Ningman Dai, Qiang Zhao, Yutong Liang, Songmei Geng, Ming Lei, Feng Xu, Lin Wang, and Bo Cheng. "Influence of Curvature on Cell Motility and Morphology during Cancer Migration in Confined Microchannels". In: *ACS Applied Materials & Interfaces* 16.8 (2024), pp. 9956–9967.

[16] Mazlee Bin Mazalan, Mohamad Anis Bin Ramlan, Jennifer Hyunjong Shin, and Toshiro Ohashi. "Effect of geometric curvature on collective cell migration in tortuous microchannel devices". In: *Micromachines* 11.7 (2020), p. 659.

[17] Gabriel Shatkin, Benjamin Yeoman, Katherine Birmingham, Parag Katira, and Adam J Engler. "Computational models of migration modes improve our understanding of metastasis". In: *APL bioengineering* 4.4 (2020), p. 041505.

[18] Bo Cheng, Min Lin, Guoyou Huang, Yuhui Li, Baohua Ji, Guy M Genin, Vikram S Deshpande, Tian Jian Lu, and Feng Xu. "Cellular mechanosensing of the biophysical microenvironment: a review of mathematical models of biophysical regulation of cell responses". In: *Physics of life reviews* 22 (2017), pp. 88–119.

[19] Revathi Ananthakrishnan and Allen Ehrlicher. "The forces behind cell movement". In: *International journal of biological sciences* 3.5 (2007), p. 303.

[20] Alberto Elosegui-Artola, Xavier Trepat, and Pere Roca-Cusachs. "Control of mechanotransduction by molecular clutch dynamics". In: *Trends in Cell Biology* 28.5 (2018), pp. 356–367.

[21] Clarence E Chan and David J Odde. "Traction dynamics of filopodia on compliant substrates". In: *Science* 322.5908 (2008), pp. 1687–1691.

[22] Ze Gong, Spencer E Szczesny, Steven R Caliari, Elisabeth E Charrier, Ovijit Chaudhuri, Xuan Cao, Yuan Lin, Robert L Mauck, Paul A Janmey, Jason A Burdick, and Vivek B Shenoy. "Matching material and cellular timescales maximizes cell spreading on viscoelastic substrates". In: *Proceedings of the National Academy of Sciences* 115.12 (2018), E2686–E2695.

[23] Partho Sakha De and Rumi De. "Stick-slip dynamics of migrating cells on viscoelastic substrates". In: *Physical Review E* 100.1 (2019), p. 012409.

[24] Kolade Adebowale, Ze Gong, Jay C Hou, Katrina M Wisdom, Damien Garbett, Hong-pyo Lee, Sungmin Nam, Tobias Meyer, David J Odde, Vivek B Shenoy, and Ovijit Chaudhuri. "Enhanced substrate stress relaxation promotes filopodia-mediated cell migration". In: *Nature materials* 20.9 (2021), pp. 1290–1299.

[25] Aleksi Isomursu, Keun-Young Park, Jay Hou, Bo Cheng, Mathilde Mathieu, Ghaidan A Shamsan, Benjamin Fuller, Jesse Kasim, M Mohsen Mahmoodi, Tian Jian Lu, Guy M Genin, Feng Xu, Min Lin, Mark D Distefano, Johanna Ivaska, and David J Odde. "Directed cell migration towards softer environments". In: *Nature Materials* (2022), pp. 1–10.

[26] Benjamin L Bangasser, Ghaidan A Shamsan, Clarence E Chan, Kwaku N Opoku, Erkan Tüzel, Benjamin W Schlichtmann, Jesse A Kasim, Benjamin J Fuller, Brannon R McCullough, Steven S Rosenfeld, and David J Odde. "Shifting the optimal stiffness for cell migration". In: *Nature Communications* 8.1 (2017), pp. 1–10.

[27] Eric J Campbell and Prosenjit Bagchi. "A computational study of amoeboid motility in 3D: the role of extracellular matrix geometry, cell deformability, and cell–matrix adhesion". In: *Biomechanics and modeling in mechanobiology* 20 (2021), pp. 167–191.

[28] Adrian Moure and Hector Gomez. "Phase-field model of cellular migration: Three-dimensional simulations in fibrous networks". In: *Computer Methods in Applied Mechanics and Engineering* 320 (2017), pp. 162–197.

[29] Elisabeth G Rens and Roeland MH Merks. "Cell shape and durotaxis explained from cell-extracellular matrix forces and focal adhesion dynamics". In: *Iscience* 23.9 (2020), p. 101488.

[30] Bahador Marzban, Jiming Kang, Ningwei Li, Yubing Sun, and Hongyan Yuan. "A contraction–reaction–diffusion model: Integrating biomechanics and biochemistry in cell migration". In: *Extreme Mechanics Letters* 32 (2019), p. 100566.

[31] Elisabeth G Rens and Leah Edelstein-Keshet. "From energy to cellular forces in the Cellular Potts Model: An algorithmic approach". In: *PLoS computational biology* 15.12 (2019), e1007459.

[32] Falko Ziebert, Sumanth Swaminathan, and Igor S Aranson. "Model for self-polarization and motility of keratocyte fragments". In: *Journal of The Royal Society Interface* 9.70 (2012), pp. 1084–1092.

[33] Amit Pathak. "Modeling and predictions of biphasic mechanosensitive cell migration altered by cell-intrinsic properties and matrix confinement". In: *Physical biology* 15.6 (2018), p. 065001.

[34] Melda Tozluoğlu, Alexander L Tournier, Robert P Jenkins, Steven Hooper, Paul A Bates, and Erik Sahai. "Matrix geometry determines optimal cancer cell migration strategy and modulates response to interventions". In: *Nature cell biology* 15.7 (2013), pp. 751–762.

[35] Wenya Shu and C Nadir Kaplan. "A multiscale whole-cell theory for mechanosensitive migration on viscoelastic substrates". In: *Biophysical Journal* 122.1 (2023), pp. 114–129.

[36] Wenya Shu and C Nadir Kaplan. "A multiscale theory for spreading and migration of adhesion-reinforced mesenchymal cells". In: *Journal of the Royal Society Interface* 20.209 (2023), p. 20230317.

[37] Yuan Li, David Lovett, Qiao Zhang, Srujana Neelam, Ram Anirudh Kuchibhotla, Ruijun Zhu, Gregg G Gundersen, Tanmay P Lele, and Richard B Dickinson. "Moving cell boundaries drive nuclear shaping during cell spreading". In: *Biophysical journal* 109.4 (2015), pp. 670–686.

[38] E Loth. "Drag of non-spherical solid particles of regular and irregular shape". In: *Powder Technology* 182.3 (2008), pp. 342–353.

[39] Carmela Rianna and Manfred Radmacher. "Comparison of viscoelastic properties of cancer and normal thyroid cells on different stiffness substrates". In: *European Biophysics Journal* 46.4 (2017), pp. 309–324.

[40] Juan Carlos Gil-Redondo, Andreas Weber, Barbara Zbiral, Vivanco Maria dM, and José L Toca-Herrera. "Substrate stiffness modulates the viscoelastic properties of MCF-7 cells". In: *Journal of the Mechanical Behavior of Biomedical Materials* 125 (2022), p. 104979.

[41] Bruce Alberts, Alexander Johnson, Julian Lewis, Martin Raff, Keith Roberts, and Peter Walter. *Molecular Biology of the Cell*. 4th. New York: Garland Science, 2002.

[42] We converted the the experimental substrate modulus E_{sub} (kPa) to the stiffness K_{sub} (pN/nm) by using the relation $K_{sub} \approx 2E_{sub}R_{FA}$, where $2R_{FA} \approx 1.0\mu m$ approximates the diameter of the nearly circular FA region [48, 49].

[43] Verena Ruprecht, Stefan Wieser, Andrew Callan-Jones, Michael Smutny, Hitoshi Morita, Keisuke Sako, Vanessa Barone, Monika Ritsch-Marte, Michael Sixt, Raphaël Voituriez, et al. "Cortical contractility triggers a stochastic switch to fast amoeboid cell motility". In: *Cell* 160.4 (2015), pp. 673–685.

[44] Jie Zhu and Alex Mogilner. "Comparison of cell migration mechanical strategies in three-dimensional matrices: a computational study". In: *Interface focus* 6.5 (2016), p. 20160040.

[45] Robert S Fischer, Xiaoyu Sun, Michelle A Baird, Matt J Hourwitz, Bo Ri Seo, Ana M Pasapera, Shalin B Mehta, Wolfgang Losert, Claudia Fischbach, John T Fourkas, and Clare M. Waternam. "Contractility, focal adhesion orientation, and stress fiber orientation drive cancer cell polarity and migration along wavy ECM substrates". In: *Proceedings of the National Academy of Sciences* 118.22 (2021), e2021135118.

[46] Aniket Jana, Katherine Ladner, Emil Lou, and Amrinder S Nain. "Tunneling nanotubes between cells migrating in ECM mimicking fibrous environments". In: *Cancers* 14.8 (2022), p. 1989.

[47] Aniket Jana, Avery Tran, Amritpal Gill, Alexander Kiepas, Rakesh K Kapania, Konstantinos Konstantopoulos, and Amrinder S Nain. "Sculpting Rupture-Free Nuclear Shapes in Fibrous Environments". In: *Advanced Science* 9.25 (2022), p. 2203011.

[48] Utku Horzum, Berrin Ozdil, and Devrim Pesen-Okvur. "Step-by-step quantitative analysis of focal adhesions". In: *MethodsX* 1 (2014), pp. 56–59.

[49] Sam Walcott and Sean X Sun. "A mechanical model of actin stress fiber formation and substrate elasticity sensing in adherent cells". In: *Proceedings of the National Academy of Sciences* 107.17 (2010), pp. 7757–7762.